Performance Enhancement of Polymer-Based Solar Cells by Induced Phase-Separation with Silica Particles

Journal:	*Journal of Materials Chemistry C*
Manuscript ID:	TC-ART-08-2014-001947
Article Type:	Paper
Date Submitted by the Author:	29-Aug-2014
Complete List of Authors:	Shen, Hao; University of Delaware, Department of Chemical and Biomolecular Engineering Valadez-P´erez, Nestor; National Institute of Standards and Technology, Center for Neutron Research Guralnick, Brett; University of Delaware, Department of Chemical and Biomolecular Engineering Liu, Yun; NIST, Mackay, Michael; University of Delaware, Department of Materials Science and Engineering

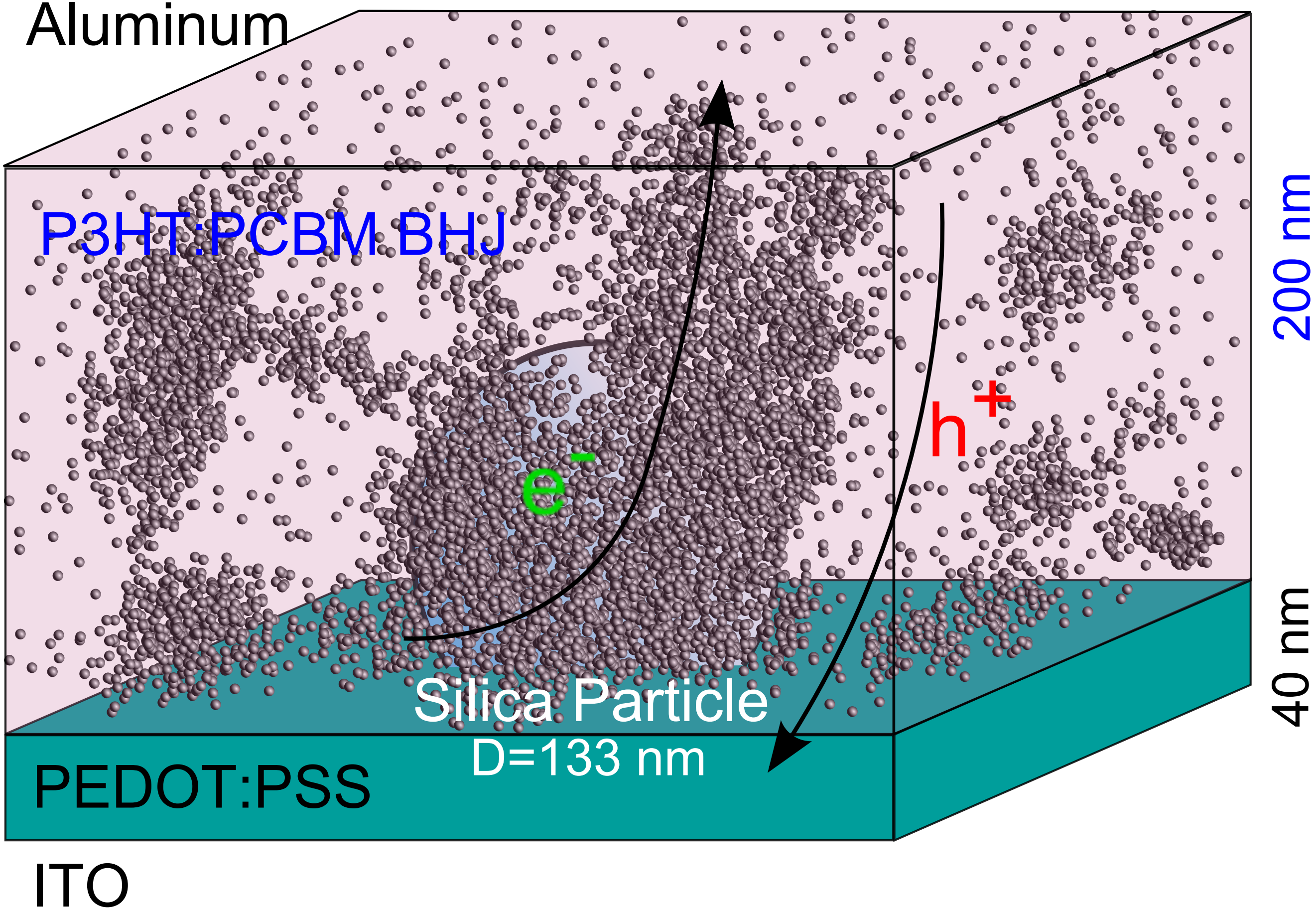
Aluminum
P3HT:PCBM BHJ
200 nm
e^-
h^+
Silica Particle
D=133 nm
40 nm
PEDOT:PSS
ITO

Performance Enhancement of Polymer-Based Solar Cells by Induced Phase-Separation with Silica Particles†

Hao Shen,[a] Néstor E. Valadez-Pérez,[b] Brett Guralnick,[a] Yun Liu,[a,c] and Michael E. Mackay[a,d*]

Received Xth XXXXXXXXXX 20XX, Accepted Xth XXXXXXXXX 20XX
First published on the web Xth XXXXXXXXXX 200X
DOI: 10.1039/b000000x

Adding metallic nanoparticles into bulk-heterojunction, polymer-based solar cells has been proven an effective strategy to enhance light absorption of the active layer and device performance. However, the high-energy surfaces on the nanoparticles may also affect the morphology of the active layer by influencing phase-separation, which has not been studied in detail. Here, we show that silica particles embedded in the active layer will affect the aggregation behavior of [6,6]-phenyl C_{61}-butyric acid methyl ester (PCBM) in the bulk-heterojunction of poly(3-hexylthiophene) (P3HT):PCBM. Using a novel graphical technique to analyze the absolute scattering intensity of small angle neutron scattering data, we conclusively demonstrate that some PCBM will migrate away from the bulk solution to the surface of the silica upon annealing and improve the device performance. The overall effect is to decrease the device series resistance and improve the power conversion efficiency by 10 to 20 % relative to the control group. In contrast to metallic nanoparticles that utilize the surface plasmon resonance, our results indicate that, even with optically inert particles, the induced phase separation of PCBM may also result in an improved device.

Introduction

Engineering a bulk-heterojunction (BHJ) polymer-based solar cell (PSC), which contains a mixture of conjugated polymer and a fullerene derivative as the active layer, requires a desirable nanoscopic morphology to achieve optimal performance.[1] The power conversion efficiency (PCE) in this category of photovoltaic devices is limited by excitonic dissociation, which happens at the interface between the electron donor (polymer) and acceptor (fullerene derivative), as well as charge transport within each component, which is greatly affected by the morphology.[2] A conventional way to make an active layer is to directly cast the polymers and fullerenes together from the solution. The morphology in these composite thin films is kinetically trapped,[3–6] representing difficulty to have the optimal domain sizes as well as an appropriate vertical distribution of the components. Therefore, the properties of the active layer are very sensitive to the process conditions, which have been extensively studied to gain control over the morphology and to improve device performance.[1,7,8]

As a complimentary approach to improve the performance, increasing the light absorption of the active layer by light scattering has been proposed in various photovoltaic technologies.[9] However, conventional methods using textures on the device surface to scatter the incident light are not effective in thin-film solar cells, because the size of light scattering structures is much larger than the thickness of the active layer (ca. 100 nm).[10,11] Therefore, there has been a strong motivation to adapt the localized surface plasmon resonance on metallic nanostructures to enhance light absorption in the thin film photovoltaics.[10–12] Silver and gold nanoparticles (NPs) are among the most popular choices due to their simple geometry and effectiveness,[13] and successful application within BHJ PSCs have been achieved. The metal NPs can be simply placed at the incident side of the device to scatter the light prior to entering the active layer.[14–22] Later, directly embedding the metal NPs inside the BHJ was demonstrated theoretically[23,24] and experimentally[25–34] to enhance the light absorption by even more. The majority of the studies reported that either approach will improve the PCE under normal AM1.5G spectrum at one sun intensity ($100\,\mathrm{mW\,cm^{-2}}$). For example, one traditional BHJ model system consisting of poly(3-hexylthiophene) (P3HT):[6,6]-phenyl C_{61}-butyric acid methyl ester (PCBM) will have an increase in PCE by 10 to 30 %,[15–18,22,30]as well as for other inherently higher-performance materials.[31–36]

While embedding gold[27] or silver[29] NPs inside

---

† Electronic Supplementary Information (ESI) available: [details of any supplementary information available should be included here]. See DOI: 10.1039/b000000x/

[a] *Department of Chemical and Biomolecular Engineering, University of Delaware, Newark, DE 19716, USA.*
[b] *División de Ciencias e Ingenierías, Campus León, Universidad de Guanajuato, Loma del Bosque 103, Lomas del Campestre, 37150 Len, Guanajuato, Mexico.*
[c] *NIST Center for Neutron Research, National Institute of Standards and Technology, Gaithersburg, MD 20899, USA.*
[d] *Department of Materials Science and Engineering, University of Delaware, Newark, DE 19716, USA. Fax: +1-302-831-4545; Tel: +1-302-831-2062; E-mail: mem@udel.edu*

P3HT:PCBM layers has achieved the highest improvements in PCE, by up to 40 %, its effectiveness is not always guaranteed. Other studies have reported worse performance[25,26] or similar 10 to 30 % improvement[30,34] that can be otherwise achieved by embedding the NPs in the poly(3,4-ethylenedioxythiophene) (PEDOT): poly(styrenesulfonate) (PSS) layer,[15–18] without undesirable effects such as the agglomeration of NPs.[25,26] The negative effects of these NPs inside the BHJ layer were also attributed to the quenching of excitons in the polymer phase by the NPs,[25,26] or the modification of the morphology in the BHJ such as disturbance of P3HT crystals, leading to inferior charge transport properties.[25,31] On the contrary, some studies reported remarkable improvement in PCE[14,20] or exciton dissociation[37] by NPs while the optical properties of the materials was enhanced marginally[20] or not at all,[14,37] and various potential positive effects were suggested.[14,20,37] Indeed, including NPs in the active layer of PSCs results in far more complicated scenarios that cannot be explained by surface plasmon resonance alone, as pointed out by Gan et al. in their comprehensive review.[11]

One important, but often overlooked aspect of NP incorporation in the active layer is their potential impact on the morphology in the BHJ, and thus it may not be true to assume the same morphology exists after the application of NPs. In a conventional BHJ active layer, a high weight ratio of fullerene is mixed with polymer. It has been known that the distribution of fullerene is sensitive to the surface in contact with a BHJ layer as well as processing conditions. In P3HT:PCBM PSCs, Campoy-Quiles *et al.* have demonstrated the importance of a lower-energy surface on PEDOT:PSS, which reduces the aggregation of PCBM onto the substrate, compared with control groups of quartz surfaces, and prevents large-scale phase separation.[38] Gomak and coworkers conducted a series of studies linking the surface energy of the substrate and the vertical segregation of the PCBM.[39–41] Because a high concentration of PCBM was found next to the PEDOT:PSS substrate, which is undesirable for the electron acceptor to be next to the cathode,[42,43] inverted device structures with metal oxide substrates[44,45] and alternative buffer layers[46] have been proposed. PCBM also tends to concentrate at the BHJ-metal interface, and therefore annealing after metal anode deposition was suggested to build a better electron transport pathway.[47–49] Considering the above evidence, we argue that surface energy plays an important role in the location of PCBM in the active layer, and hypothesize that embedding NPs in the active layer may potentially change its morphology.[50] Such change could influence the performance of the device, which has not been fully considered as of yet. Hence, it is essential to separate and study the morphological changes induced by high-energy surfaces on the nano-structures from their optical contribution.

In this report, we study the influence of electrically and optically inert silica particles on the morphology of the BHJ and device performance. We want to use them to construct a predefined device architecture, and use their high-energy surface (surface energy of silica is 77.4 mN/m^2 compared to 45.7 mN/m^2 for PEDOT:PSS)[39] to manipulate the distribution of PCBM in the P3HT:PCBM active layer.[38,40,42,44,51–53] This approach is complimentary to Liao *et al.*'s method, where they incorporated small (5 nm) Cu_2S and CdSe NPs into the BHJ layer to tune the aggregation of PCBM.[50] Here large (133 nm) diameter silica particles were chosen specifically because they scatter negligibly near the absorption edge of P3HT at a wavelength of 650 nm. Moreover, this material is also an electrical insulator, so the particles only introduce high-energy surfaces without any electro-optical contribution. In addition, such a size is near the thickness of a conventional active layer, so they are expected to direct the assembly of PCBM across the film, and possibly achieve better transport properties between the electrodes. These attributes make silica particles an ideal candidate to examine our hypothesis that structures embedded within the active layer can influence the morphology of the active layer.

Results and Discussion

Size and surface distribution of silica particles

A traditional PSC employs PEDOT:PSS as the buffer layer between the P3HT:PCBM active layer and the conductive oxide substrate. Here we spun-coat silica particles together with the PEDOT:PSS solution to modify the device architecture, as described in the experimental section. The silica particles were both characterized at the dilute colloidal state in D_2O, and after deposition with PEDDOT:PSS on the the silicon wafers. Figure 1 (a) shows the small angle neutron scattering (SANS) data of the dilute colloids, and deposited silica particles with PEDOT:PSS. The PEDOT:PSS layer is thin (40 nm) compared to the average diameter of the particles (133 nm), and its scattering was subtracted as the background along with that due to the silicon wafers. Therefore, the particles coated with PEDOT:PSS are essentially suspended in the ambient air in terms of the scattering experiment.

We observe two major differences in the data of coated particles from the colloidal counterpart. One is the absence of the incoherent background because the scattering of PEDOT:PSS was subtracted already, and the other is the formation of an inter-particle structure at low q (scattering vector, $q = 4\pi \sin\theta/\lambda$) due to particle aggregation during the spin-coating process. By using a Guinier analysis, the radii of gyration for the dilute colloids and the coated particles can be determined as 55.9 and 95.9 nm, respectively. Adopting the spherical geometry, the former value yields an average radius

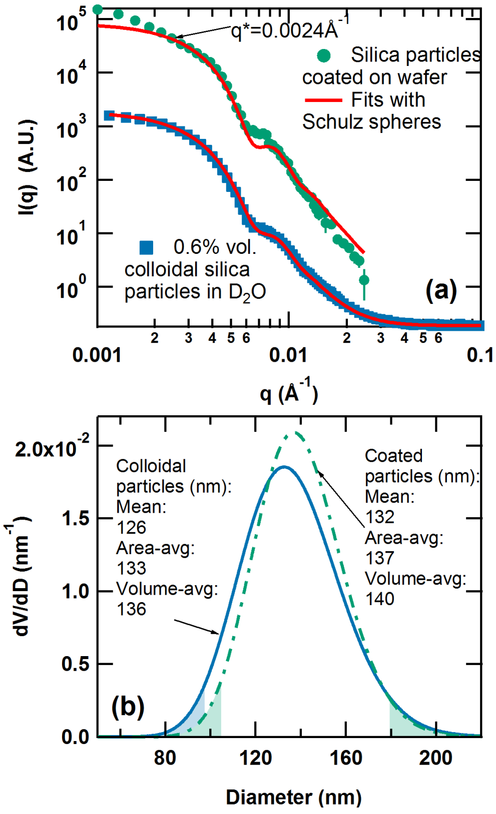

Fig. 1 (a) SANS data of silica particles being dilute colloids and coated onto silicon wafers with PEDOT:PSS. The solid lines indicate the best fits with spherical form factor with a Schulz size distribution. The scattering vector $q*$ ($q* = \pi/4R$) is an arbitrary cut-off value for fitting, where R is the average radii of the particles. (b) Volumetric distribution function from the fits. The shaded area indicates the portion outside the 95 % interval.

of 72.2 nm. Judging from the fact that the radius of gyration of the coated particles is only moderately increased from the radius of the spheres, a significant portion of them were individually dispersed onto the surface, which will be discussed in more detail below.

Moreover, at sufficiently large q, the SANS intensity of the coated silica particles enters the Porod region showing a spherical form factor. Therefore, the data above $q* = \pi/4R$, an arbitrary cut-off value where R is the average radii of the particles, was fitted with a spherical form factor with a Schulz size distribution.[54] Fitting the data with this model is hereafter called the Schulz spheres model. The data of the dilute colloidal solution was also fitted throughout its whole range of q, and the volumetric distribution functions derived from the fitting results are shown in Fig. 1 (b). We therefore conclude the coating process only slightly increases the apparent size of the particles, which may be a result of some aggregation during the process. Regardless, the form factor of the particles remains remarkably similar after coating. This finding serves as the basis of further discussion on more complicated scattering patterns where the additional P3HT:PCBM layer is involved.

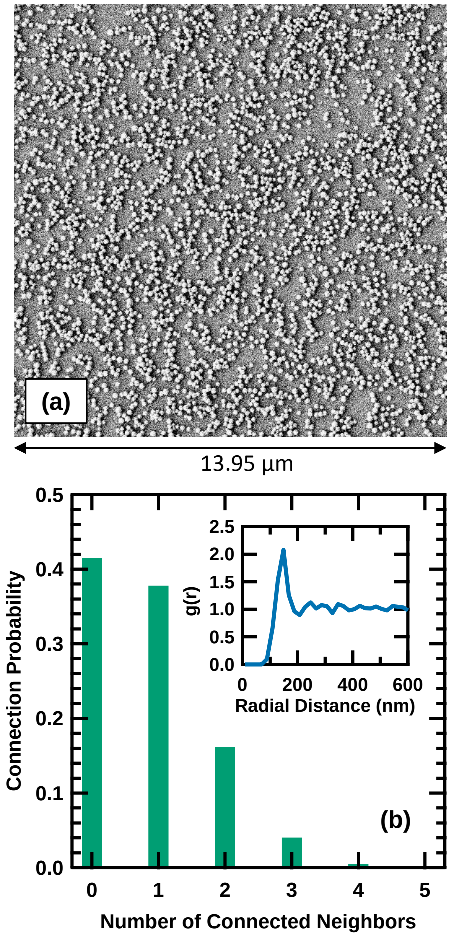

Fig. 2 (a) Top-down SEM image of coated silica particles with PEDOT:PSS on a silicon wafer. (b) Connection probability as a function of the number of connected neighbors. The insert is the radial distribution function.

To further confirm the silica particles are evenly distributed, their scanning electron microscopy (SEM) images were taken as shown in panel (a) of Fig. 2, where the particles are found to form a single layer. We also confirmed by x-ray photoelectron spectroscopy (XPS) that the PEDOT:PSS layer does not cover all the surface of the silica particles, so some of the silica surface is exposed (see Supporting Information). On this $13.95 \times 13.95\,\mu m^2$ sampling area, center coordinates of 3526 particles were manually traced, yielding a surface number density of $18.1\,\mu m^{-2}$. By using the area average diameter of 133 nm, the projected surface coverage is estimated as

~25 %. To quantitatively evaluate the distribution of the particles, the radial distribution function was calculated, shown in the insert of Fig. 2 (b).[55] Its first minimum is taken as the correlation distance, σ (208 nm). We assume two particles connect when their center-to-center distance is less than 1.1 σ, and define the connection probability as the ratio of numbers of connected particles to the total population. Figure 2 (b) shows the connection probability as a function of the number of connected neighbors. One can determine there are ~40 % of the particles that did not connect with any other, and about the same amount connected with only one neighbor, which together constitute the majority of the population. By using this analysis, we have shown most particles were sparsely distributed on the surface.

Optical properties of silica particles

A cross-sectional SEM image of a solar cell filled with silica particles without the aluminum electrode is shown in Fig. 3 (a). The substrate of the device is indium-tin oxide (ITO) glass coated with PEDOT:PSS and the silica particles. One can observe that the active layer can wet the silica particles entirely, and the geometry of the device is minimally affected by the presence of silica particles.

The light scattering of silica particles were measured by UV-Vis spectra as shown in Fig. 3 (b). Both the plain and silica-modified version of the PEDOT:PSS layer has very low absorbance. Since the absorbance was measured in the direct path of the light source, some light was scattered off the path to the photon detector, which is interpreted as the increased absorbance. However, such scattering has very little effect compared with the magnitude in the absorbance of the active layer, and the affected wavelength is below 400 nm, far from the main absorption edge of P3HT at 580 nm. Therefore, both the absorption spectra of the active layer with and without silica particles are very similar. However, there is some slight different at the shoulder around 600 nm for the as-cast samples, which is related to the inter-chain packing of P3HT.[56] The silica particles may have affected the film forming dynamics during the casting process and caused such a subtle difference, but was eliminated later by thermal annealing. Therefore, we conclude silica particles have negligible effects on the light absorption of the active layer.

Morphology of P3HT:PCBM active layers

Before considering the effect of silica particles on the morphology of the P3HT:PCBM active layer, the morphology of the control samples without the silica should be studied. It has been known that these two materials phase separate upon film formation to make structures on the order of 10 nm in size. Those structures are often characterized as the crystals of P3HT, clusters of PCBM (whether crystalline or not), and some blend of amorphous P3HT mixed with PCBM. In the studies using scattering techniques, simplified two phase models are often assumed to describe the active layer.[3,6,57,58] Based on previous studies, the contrast between the crystalline and amorphous P3HT is too low to be distinguished using SANS in the solid state,[3,6] and the PCBM phase contains very little, if any, P3HT. Therefore we assume there is one phase that is pure PCBM, and the other matrix phase made up with crystalline and amorphous P3HT together with dispersed PCBM.

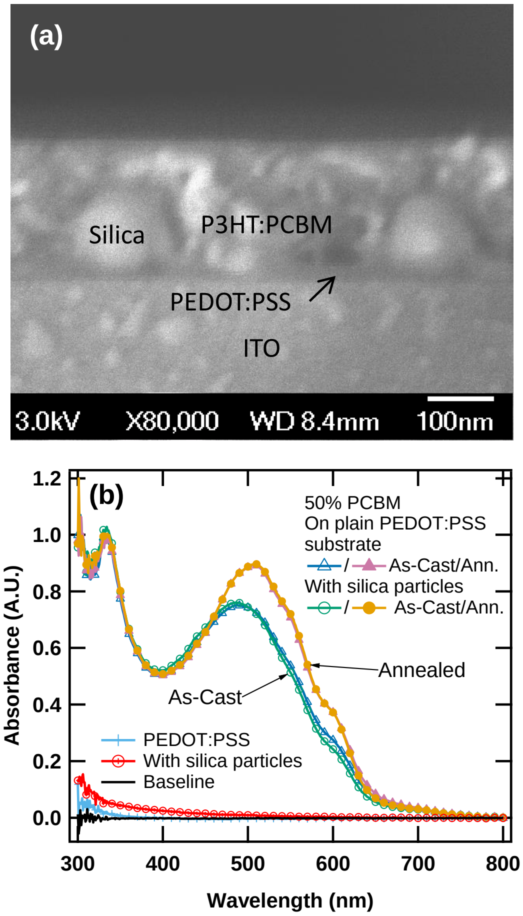

Fig. 3 (a) Cross-sectional SEM image of the active layer cast onto a PEDOT:PSS substrate decorated with silica particles. (b) UV-Vis absorbance spectra of 50 Wt.% PCBM in the P3HT:PCBM active layer. The open symbols represent as-cast samples and closed ones annealed at 110 °C. There is no significant gain in the absorbance of the active layer upon addition of silica particles.

The SANS data of the P3HT:PCBM blends at different PCBM contents is presented in Fig. 4, before and after annealing at 110 °C for 10 minutes for the same sample. We found the scattering data can be well described by the Teubner-Strey

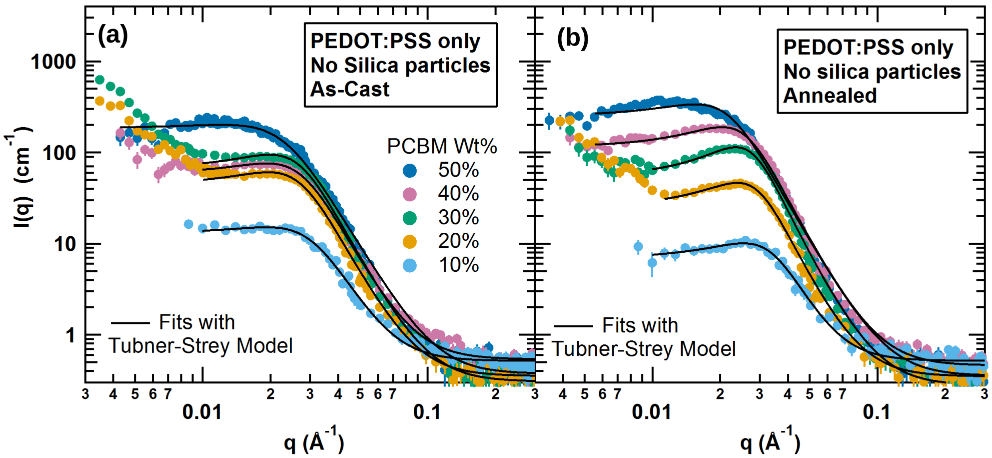

Fig. 4 SANS data of the P3HT:PCBM on the PEDOT:PSS substrates without silica particles (a) As-Cast samples. (b) Annealed at 110 °C.

model,[6,58–60] which is represented by the following equation for a two-phase bicontinuous mixture:

$$I(q) = \frac{\phi_p(\Delta\rho)^2(\frac{8\pi}{\xi})}{\frac{a_2}{c_2}+\frac{c_1}{c_2}q^2+q^4}+Bkg \tag{1}$$

This model has the following fitting parameters: a_2, c_1, c_2, ϕ_p (the volume fraction of PCBM phase), $\Delta\rho$ (the contrast in the scattering length densitiess (SLDs)) and Bkg (the incoherent background). Two characteristic lengths can be extracted from the fitting parameters: the repeat distance d, the average distance between the two phases, and the correlation length ξ:[60]

$$d = 2\pi\left[\frac{1}{2}\left(\frac{a_2}{c_2}\right)^{\frac{1}{2}}-\frac{c_1}{4c_2}\right]^{-\frac{1}{2}} \tag{2}$$

$$\xi = \left[\frac{1}{2}\left(\frac{a_2}{c_2}\right)^{\frac{1}{2}}+\frac{c_1}{4c_2}\right]^{-\frac{1}{2}} \tag{3}$$

The characteristic lengths from the models are summarized as functions of PCBM concentration in Fig. 5. One can readily see the repeat distance shows a strong dependence on the PCBM concentration as previously reported in a similar system.[6,58] Because some PCBM is inevitably trapped with the amorphous P3HT mixture, complete phase-separation is unlikely.[3,6,61,62]. As a result, when the PCBM concentration is much greater than the equilibrium miscibility of these two materials, more PCBM segregates and participates in the formation of the nano-structure thereby increasing the repeat distance. On the other hand, we observe the correlation length is rather constant across the concentration range of PCBM, around 10 nm. This quantity is a measure of the distortion of the interfaces. According to Vonk *et al.*'s definition, it is the average distance traveled within one phase along a plane parallel to the starting point's nearest interface, before hitting the interface.[60]. Since ξ is much smaller than d, this implies the boundaries between the two phases lack long-range order, which has been found in many other studies with microscopy.[1,63]

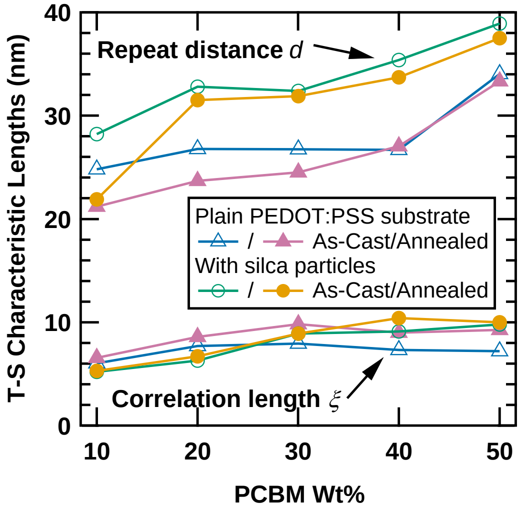

Fig. 5 Characteristic lengths derived from the Teubner-Strey model. The error bars represent the uncertainty of the estimation from the data fitting. However, most of them are smaller than the size of the markers.

Morphology of the active layer containing silica particles

Now consider the SANS of the P3HT films containing silica particles. The SANS data for P3HT films without PCBM are shown in Fig. 6. These films were spun-coated onto silicon wafers decorated with silica particles in the PEDOT:PSS layer, and the absolute intensity was scaled according to the thickness of the P3HT films (320 nm). The scattering data for the silica particles in Fig. 1 is also plotted here and vertically offset for ready comparison. As one can clearly see, although the particles aggregate slightly due to the coating process, the Porod behavior in the scattering pattern is not affected. Therefore, we can safely conclude that the scattering of the silica particles is similar to the dilute colloids in the Porod regime above q =0.003 $Å^{-1}$. Moreover, addition of a P3HT layer only contributes to the incoherent background because of its hydrogen-rich nature, and no coherent scattering is observed. Therefore, while the density difference between crystalline and amorphous P3HT may exist, there is not enough contrast for coherent scattering, as previously discussed.[3]

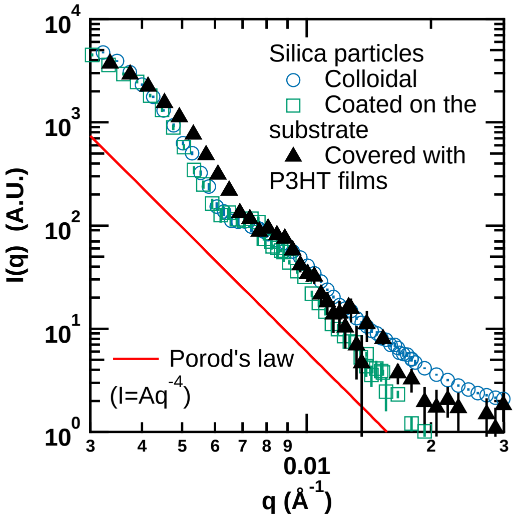

Fig. 6 SANS data of silica particles within the P3HT films. The data in Fig. 1 are also re-plotted and vertically offset for comparison. All the data follow Porod's law.

The SANS data of the active layer on top of the PEDOT:PSS substrates decorated with silica particles are shown in Figs. 7 (a) and (b). Based on previous observations, the scattering appears to be a combination of silica particles and the PCBM phase in the active layer. Thus, a summed model of the Schulz spheres and Teubner-Strey models can be fitted to those profiles (see Supporting Information). However, we must note that the Schulz sphere form factor here is different from the cases in Fig. 6. The SLDs of silica, PCBM, and P3HT is 3.67×10^{-6}, 3.60×10^{-6} and 0.74×10^{-6} $Å^{-2}$, respectively. Therefore, one can expect when PCBM is added to the P3HT film, the contrast between the silica particle and the surrounding medium is reduced. This is the reason why the scattering from the silica particles at low q is less intense in the active layer containing PCBM.

Moreover, for the samples with the most dilute PCBM concentration of 10 Wt.%, the scattering of the silica particles and the PCBM phase is separated by approximately half a decade in q, and Porod's law for the silica particles is still followed. However, as the concentration of PCBM increases, not only does the scattering intensity from the precipitated PCBM clusters increase, but the Porod boundary of silica is less clearly seen. Specifically, the power law around 0.006 $Å^{-1}$ decreases from 4 to lower values when the PCBM concentration is greater than 10 Wt.%. Since the SLD of silica and PCBM are very close, they appear to be the same material in terms of neutron scattering. Therefore, the reduction in the order of the power law means PCBM is forming surface fractals near the surface of silica particles, some of which may even form larger structures together. Unfortunately, since the scattering vector in the experiment could not reach small values to characterize such large structures, this part of the fitting results cannot be analyzed quantitatively.

Despite the lack of quantitative insights from the Schulz spheres part of our model, it accounts for the low q scattering excellently. In some sense, it is used as a method to remove the scattering contribution of large silica-PCBM structures from the SANS data, allowing detailed analysis of the PCBM phase at the nano-scale above a scattering vector of 0.01 $Å^{-1}$ (smaller than 62.8 nm in real space). As shown in Figs. 7 (a) and (b), the summed model fits all the data sets throughout the entire q range. Panels (c) and (d) below show the residual data after subtraction of the Schulz sphere contribution from the original data, and the lines are the plotted Teubner-Strey model using fit parameters obtained in the summed model. As shown in Fig. 5, the same characteristic lengths can be extracted from the Tebner-Strey parameters. One can see the repeat distance follows the same trend with concentration of the PCBM, but is systematically larger than the control group without the silica, while the correlation length is unaffected.

We believe such an increase in d is really due to the presence of silica particles producing a very different morphology. Note, the uncertainty of d estimated from Teubner-Strey model is insignificant compared to the change induced by silica particles because error bars in Fig. 5 are smaller than the size of the markers. Also, we can directly confirm the disparate peak positions between Fig. 4 (b) and Fig. 7 (b), so the increase in d in the presence of silica particles is certain. A larger repeat distance between the PCBM phase and the matrix implies the they are separated further and form more distant domains. This complies with our theory that the silica particles attract the PCBM. Because PCBM is forced to con-

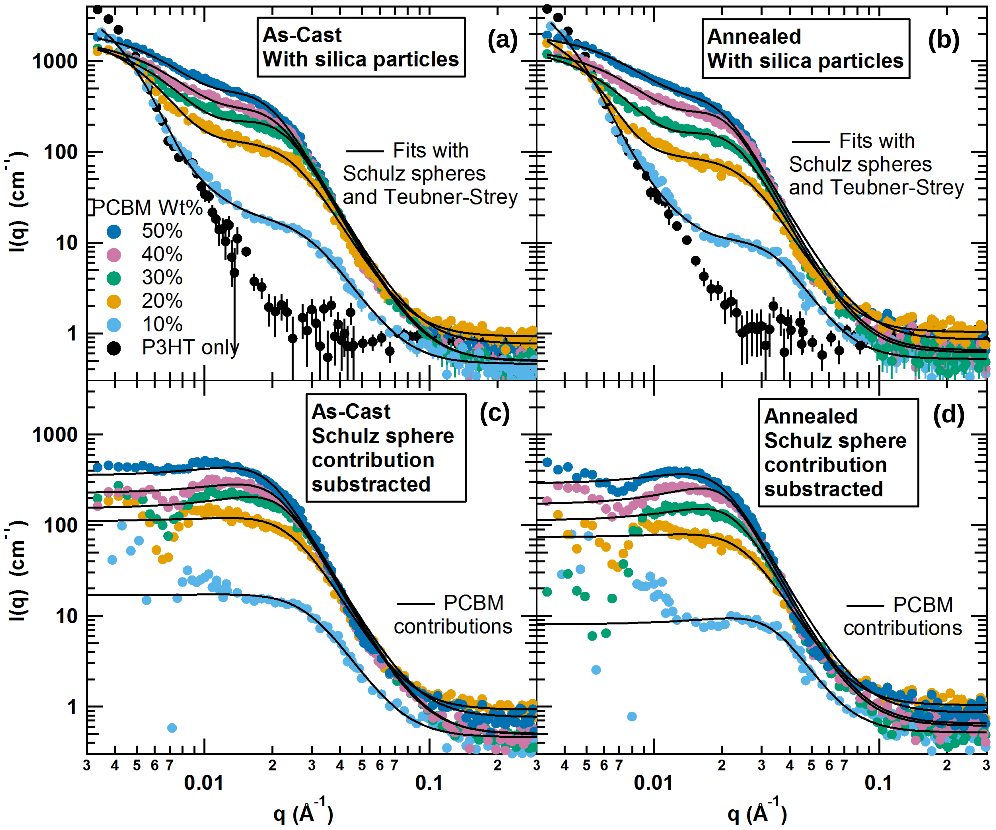

Fig. 7 SANS data of the P3HT:PCBM on the PEDOT:PSS substrates with silica particles (a) As-Cast samples. (b) Annealed at 110 °C. (c), (d) Same data as the above panels after subtraction of the contribution from the Schulz sphere model.

centrate around the surface of the particle, some other regions will become depleted of PCBM, and the average space between the two phases can become larger.

Change of scattering intensity upon annealing

The strongest evidence that the silica particles affect the morphology of the BHJ is how the scattering intensity is changed upon annealing. Thermal annealing of these mixtures is known to drive their morphology away from their trapped, as-cast state. As shown in Fig. 4, the scattering intensity is increased by thermal annealing when the PCBM content is greater than or equal to 30 Wt.%. This is because at higher concentration, PCBM tends to diffuse out of the matrix and aggregates to form more PCBM-rich phase. The former part increases the scattering contrast, $\Delta\rho$, while the latter increases the volume fraction of the PCBM phase, ϕ_p, both of which enhance the overall scattering intensity of the system.[3,6,61] On the contrary, the intensity in the cases with 10 and 20 Wt.% PCBM decreases slightly upon annealing, because there may be favorable mixing entropy for the particles to dissolve in the polymer.[64]

However, in the presence of silica particles, the intensity is decreased after annealing in all cases as shown in the lower panels in Fig. 7, in contrast to the control group with the opposite behavior at higher PCBM concentrations. This is a strong indication that silica particles effectively change the aggregation of PCBM, and we believe that the reason is due to the decrease in the observable amount of PCBM. If our hypothesis is true, that PCBM is forming structures with silica particles, they can be too large to be observed on the SANS spectra. As mentioned previously, this is possible since some studies had concluded high energy surfaces would cause a local increase in PCBM concentration.[38–43] Furthermore, deviation from Porod's law at low q upon addition of PCBM hints at the same result. Thus, it is likely for the silica-PCBM complex to shift out of the SANS spectrum, and reduce the scattering intensity of the PCBM-rich phase at the nano-scale above a scattering vector of 0.01 Å^{-1}.

In order to prove this hypothesis, the volume fraction of PCBM phase at the nano-scale needs to be evaluated analytically. The absolute scattering intensity is determined together by ϕ_p and $\Delta\rho$ (see Eqn. 1). A scattering experiment is commonly designed to control either one as a known variable, and use the absolute intensity to determine the value of the other. Unfortunately in our system, we have control over neither because both are subject to the extent of phase-separation during processing. Therefore, an additional constraint is necessary to determine ϕ_p and $\Delta\rho$ independently from the absolute intensity. Kiel *et al.* and Shen *et al.* have suggested to use the mass conservation of PCBM from the cast solution to determine both values.[3,6] This approach is explained briefly below, and the derivation of the equations is left to the Supporting Information.

Once the scattering data on an absolute scale is fitted to a known function, its magnitude of intensity is evaluated using the fitting parameters. For example, considering Eqn. 1, while the shape of the function is determined by a_2, c_1 and c_2, its scaling is only dependent on $\phi_p(\Delta\rho)^2$. To simplify the discussion, we define a scale factor, SF, as:

$$SF = \phi_p(\Delta\rho)^2 = \phi_p(1-\phi_m{}')^2(\rho_{PCBM} - \rho_{P3HT})^2 \qquad (4)$$

Here we also substituted $(\Delta\rho)^2$ with the expression for ϕ_m', the volume fraction of PCBM mixed in the P3HT matrix with respect to the volume of the matrix. In other words, ϕ_m' is the miscibility of PCBM in P3HT. The symbols ρ_{PCBM} and ρ_{P3HT} represent the SLDs of the respective pure materials.

The conservation of PCBM mass implies the composition in the BHJ layer determined by SANS is the same as that of the solid content in the cast solution. That is, all of the PCBM will participate in the scattering of neutrons, and what had not phase-separated to form the PCBM-rich phase (ϕ_p) must be left and trapped in the P3HT matrix ($\phi_m{}'$). Defining the bulk volume fraction of PCBM in the solid content of the cast solution as ϕ^*, this relationship can be written as:

$$\phi^* = \phi_m{}'(1-\phi_p) + \phi_p \qquad (5)$$

Given Eqns. 4 and 5, ϕ_p and $\phi_m{}'$ can be calculated from the scattering intensity.

However, in the presence of silica particles, large PCBM-silica structures may not be apparent at larger scattering vectors used in the experiment. Therefore, the amount of PCBM shown in the SANS spectra may appear to be less than ϕ^*. Eqn. 5 should be hence modified to:

$$\phi^* \geq \phi_m{}'(1-\phi_p) + \phi_p \qquad (6)$$

This generalized mass conservation relationship can provide a range of possible values in ϕ_p and $\phi_m{}'$ for a given ϕ^*, which will be used to discuss the hypothesis proposed above.

Graphical solution to the volume fraction and miscibility of PCBM

We have pointed out the evaluation of ϕ_p and ϕ_m' from the scattering intensity is not a trivial problem for such a complex system, so a new graphical approach is proposed to simplify the analysis. Figure 8 is constructed with ϕ_p as the x-axis, which is the phase-separated PCBM, and ϕ_m' as the y-axis, which is the miscibility of PCBM in the matrix. This graph is layered with two sets of contour curves. The first set is the scale factor, SF, as a function of (ϕ_p, ϕ_m'), calculated according to Eqn. 4. Notice that the calculated SF is the theoretical prediction of the scattering intensity for *any two phases*. In this study, we extracted this information from the fit parameters in the Teubner-Strey model, but it can also be any model, or calculated from the scattering invariant if the range and quality of the data permits.[61] Any additional physical limitation, in this case the conservation of mass from the cast solution, is then added independently onto the graph according to Eqn. 5. The crossing between the curves of SF and overall PCBM concentration (ϕ^*) gives the values of ϕ_p and ϕ_m'. If the total amount of PCBM is observed by SANS, the total apparent mass of PCBM in the SANS data should be ϕ^*, so the coordinates at the crossing of ϕ^* and SF correspond to ϕ_p and ϕ_m'. Otherwise, if some PCBM forms large structures falling outside the size range observable by SANS at larger q, only a partial amount of PCBM in the cast solution contributes to the SANS intensity (Eqn. 6). Therefore, the total PCBM concentration would appear to be less than ϕ^*, and the lower left segment of the SF contour to the crossing gives the range of possible answers. For example, if the nominal PCBM concentration is 50 Wt.% and SF is 1.8×10^{-12} Å^{-4}, the dashed curve emanating from the crossing is the possible combination of ϕ_p and $\phi_m{}'$, and ϕ_p is estimated to be between approximately 0.22 and 0.34.

By using Fig. 8, we can study ϕ_p and ϕ_m' intuitively. Firstly, the difference in the absolute scattering intensities between as-cast (open symbols) and annealed samples (closed symbols) is obvious. If the active layer is annealed on the plain PEDOT:PSS substrate (triangles), the SF increases when the overall PCBM composition is more than 30 Wt.%. Assuming mass conservation in these cases, one can read the values of ϕ_p and ϕ_m' at the crossings, and conclude the nanoscopic PCBM phase-separation is enhanced by annealing with more than 30 Wt.%, while the aggregated PCBM slightly dissolves back into the matrix when the concentration is under 20 Wt.%. Moreover, we recognize the outlying as-cast 40 Wt.% PCBM data point (also see the abnormally low intensity in Fig. 4 (a)), but it fell back in between other data points once annealed. It may be due to some unexpected events affecting the kinetically trapped state during the sample preparation and was reproducible. Regardless, thermal annealing eliminates this abnormality, and enhances the phase-separation when the PCBM concentration is above 30 Wt.% on the plain PEDOT:PSS substrate.

On the other hand, SF decreases significantly after annealing in all the samples with silica particles (circles). As previously discussed, the total apparent mass may not be conserved,

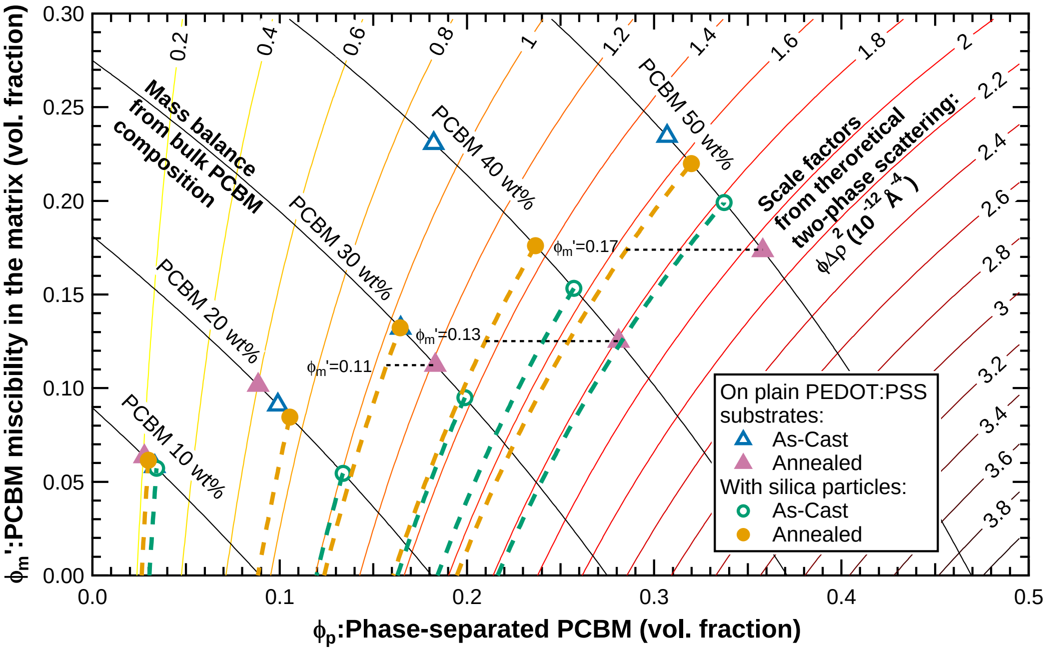

Fig. 8 Graphical analysis of the volume fraction (ϕ_p) and miscibility of PCBM (ϕ'_m). This graph contains two sets of contour curves: 1. Scale factor, *SF*, based on theoretical scattering intensity between two phases. $SF = \phi_p \Delta\rho^2 = \phi_p(1-\phi_m{}')^2(\rho_{PCBM}-\rho_{P3HT})^2$ (Eqn. 4), where ρ_{PCBM} and ρ_{P3HT} are the SLDs of PCBM (3.6×10^{-6} Å^{-2}) and P3HT (0.7×10^{-6} Å^{-2}), respectively.[52] 2. Mass balance from the bulk volume fraction of PCBM in the solid content of the cast solution, ϕ^*. $\phi^* = \phi_m{}'(1-\phi_p)+\phi_p$ (Eqn. 5). To use this graph, one should first calculate *SF* from the scattering intensity in each SANS data set, and find the corresponding *SF* contour curve. Then, according to the PCBM concentration in the cast solution, find the curve of ϕ^*. If there is no large-scale segregation, all the PCBM in the solution will appear at the nano-scale and contribute to the SANS intensity, so the total mass would be conserved. Thus, the crossing coordinates of the two curves give the values of ϕ_p and ϕ'_m. If large-scale segregation occurs, some PCBM will not contribute to the SANS intensity, and the apparent total mass shown in the SANS spectra would be less than ϕ^*. Therefore, the coordinates of any point on the the same *SF* contour curve to the left of the crossing can be the answer.

so any point on the lower left segment of the *SF* contour can be a possible answer, drawn as the dashed curves. One should pay special attention to the cases with 20 and 30 Wt.% PCBM, because there is no overlap in the possible ranges of ϕ_p between the as-cast and annealed data for these two cases. This means the decrease in the scattering intensity after annealing must be caused by the disappearance of aggregated PCBM at the nano-scale, instead of re-mixing back into the P3HT matrix. Therefore, the large-scale phase separation of PCBM must happen in the presence of silica particles in these two cases.

Moreover, the trend in the y-values of the annealed samples without silica (closed triangles) shows the dependence of miscibility between P3HT and PCBM on the bulk composition of PCBM. Previous studies have reported their miscibility using various techniques[3,4,58,62,65–68]. For 50 Wt.% blends of PCBM and P3HT, approximately 20 Vol.% of PCBM is miscible with P3HT,[3,62,67] but this value also depends on the regioregularity,[66] temperature[66] and the concentration of PCBM.[68] In particular, our results here agree with Chen *et al.*, where they use neutron reflectometry to measure the equilibrium miscibility as a function of bulk concentration of PCBM in the bilayer films of PCBM and regioregular P3HT.[68] We argue that the miscibility indeed depends on the abundance of PCBM in the system, which can vary from as little as ∼5 % at the dilute limit with PCBM, all the way to ∼20 % in the concentrated cases. For the 50 % PCBM system, ϕ'_m is found to be 17 Vol.% in this study. The concentration dependence of the miscibility is because of the complicated morphology in a BHJ influenced by the presence of crystalline P3HT, the mixture of amorphous P3HT with PCBM, and segregated PCBM domains. Therefore, the miscibility estimated directly from the Flory-Huggins coefficient might be too simple to be realistic.[58].

If ϕ'_m in the annealed samples without silica particles is assumed to represent the equilibrium miscibility of PCBM, regardless of whether silica is present or not, the amount of reduction of the nano-scaled PCBM phase due to the embedding of silica particles may be estimated. To do so, ϕ'_m is obtained from the annealed control group without silica particles at 30, 40 and 50 Wt.% PCBM and then used to determine the ϕ_p in the samples with silica particles after annealing. The data with 10 and 20 Wt.% PCBM are not discussed because both the segregated PCBM volume is not significantly different with the presence of silica particles. This calculation can be easily done by drawing horizontal lines representing the equilibrium ϕ'_m values in Fig. 8. For example, the sample with 50 Wt.% PCBM after annealing is assumed to have an equilibrium ϕ'_m of 0.17, so its corresponding ϕ_p with silica particles is 0.29. After annealing, ϕ_p at 30, 40 and 50 Wt.% is found to be 0.18, 0.28 and 0.36 in the control group, but reduces to 0.16, 0.21 and 0.29 with silica particles, respectively. Therefore, the volume of phase-separated PCBM at the nano-scale is effectively reduced by silica particles due to the formation of large silica-PCBM structures.

Liao *et al.* also reported the suppression of PCBM nano-scale phase separation with the addition of 5 nm Cu_2S NPs, where they have suggested that NPs intercalate with P3HT chains and retard the diffusion of PCBM from the matrix, and the chance to form clusters.[50] However, this mechanism cannot be true in our system because the size of silica particles is much larger than the size of P3HT chains.[69] While the mechanism on the reduction in the nano-scaled scattering intensity of PCBM remains an open question and encourages further study, it is evident that the addition of NPs has a significant effect on the BHJ morphology despite their size. This offers a strategy to gain control over the morphology as well as enhance its thermal stability,[28,29,50] and should not be neglected when the plasmonic effect is considered.

Performance enhancement of the solar cells

So far we have proven the silica particles have a definitive effect on the morphology in the P3HT:PCBM active layer, and it is critical to study its influence on the performance of the solar cells. We systematically compare the performance of the devices filled with silica particles to the control group without them. The bulk PCBM composition in the active layer was varied from 20 to 80 Wt.%, and all the solar cells here were annealed prior to the deposition of aluminum. The statistics of the device performance were determined from IV curve data of 3 to 8 devices and summarized in Fig. 9. The power conversion efficiency and series resistance are also listed in Table 1.

One can observe the PCE of the solar cells is enhanced by the silica particles when the PCBM content is equal to or greater than 50 Wt.%. In particular, the PCE can be improved by 10 to 20 % compared with the control group as shown in Table 1. The improvement in PCE mainly comes from the much better fill factor (Fig. 9 (d)), compared with the changes in the short-circuit current and open-circuit voltage (Figs. 9 (b) and (c)). The later two variables are similar because the embedded silica particles do not increase the light absorption of the device, nor does it change the band gaps of the materials. Instead, the rearrangement of the PCBM and perhaps the P3HT matrix phase in the active layer directly affects the fill factor, which is an indication of how the maximum power output deviates from the maximum value due to the influence of internal resistances. The IV curves of devices with 50 to 70 Wt.% PCBM are displayed in Fig. 10. The data of each treatment was chosen to be representative of the average PCE within the group. The effect of a higher fill factor can be seen in the improved squareness of the curve, allowing the device to operate at a point with higher output power when the silica particles are present. Moreover, the photo current is also slightly higher, especially in the cases with 60 and 70 Wt.% of PCBM. Currently we do not have a definite explanation for the increased current, but it is possible that the change of PCBM aggregates within the BHJ can also alter its quantum efficiency.[61]

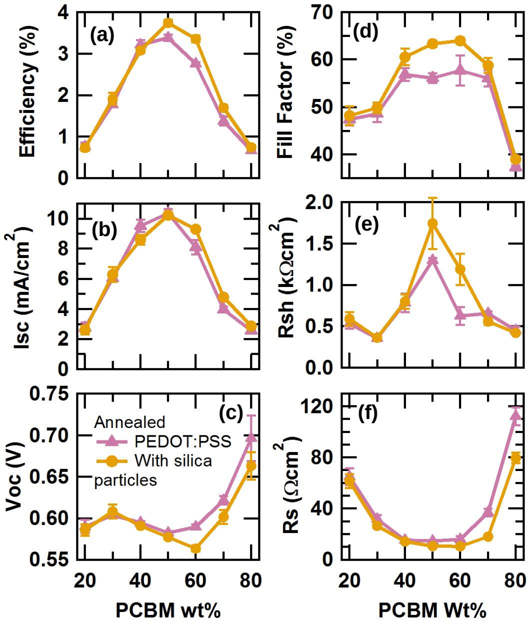

Fig. 9 Statistics of the device performance extracted form the IV curves. Each data point was the average value of 3 to 8 duplicates. (a) Power conversion efficiency at AM 1.5 illumination. (b) Short-circuit current (I_{SC}). (c) Open-circuit voltage (V_{OC}). (d) Fill factor (FF). (e) Shunt resistance (R_{sh}). (f) Series resistance (R_s).

Interestingly, the series resistance of the devices is *decreased* by as much as 50 % after being filled with the insulating silica particles, as shown in Table 1. The series resistance was calculated by taking the inverse of the derivative of the IV curve at the zero current point. As shown in the top-down SEM image in Fig. 3 (a), the particles cover the electrode by about 25 %, which is expected to block some of the current conductive pathways between the active layer and the

Table 1 Selected statistics of device performance

PCBM	Power Conversion Efficiency (%)			Series Resistance ($\Omega\,cm^2$)		
wt.%	control	w/silica	change	control	w/silica	change
20	0.76 ± 0.10	0.73 ± 0.08	−4.8 %	65.0 ± 6.6	61.3 ± 5.4	−5.7 %
30	1.77 ± 0.06	1.91 ± 0.14	+7.8 %	31.8 ± 2.9	26.5 ± 1.9	−17 %
40	3.21 ± 0.11	3.07 ± 0.05	−4.3 %	15.2 ± 0.6	14.3 ± 1.0	−6.1 %
50	3.38 ± 0.08	3.74 ± 0.08	+11 %	14.7 ± 0.7	10.6 ± 0.4	−28 %
60	2.75 ± 0.03	3.35 ± 0.08	+22 %	15.8 ± 2.6	10.3 ± 0.9	−35 %
70	1.37 ± 0.10	1.69 ± 0.07	+23 %	36.7 ± 2.9	18.1 ± 1.2	−51 %
80	0.67 ± 0.05	0.74 ± 0.05	+11 %	112 ± 69	79.5 ± 4.3	−29 %

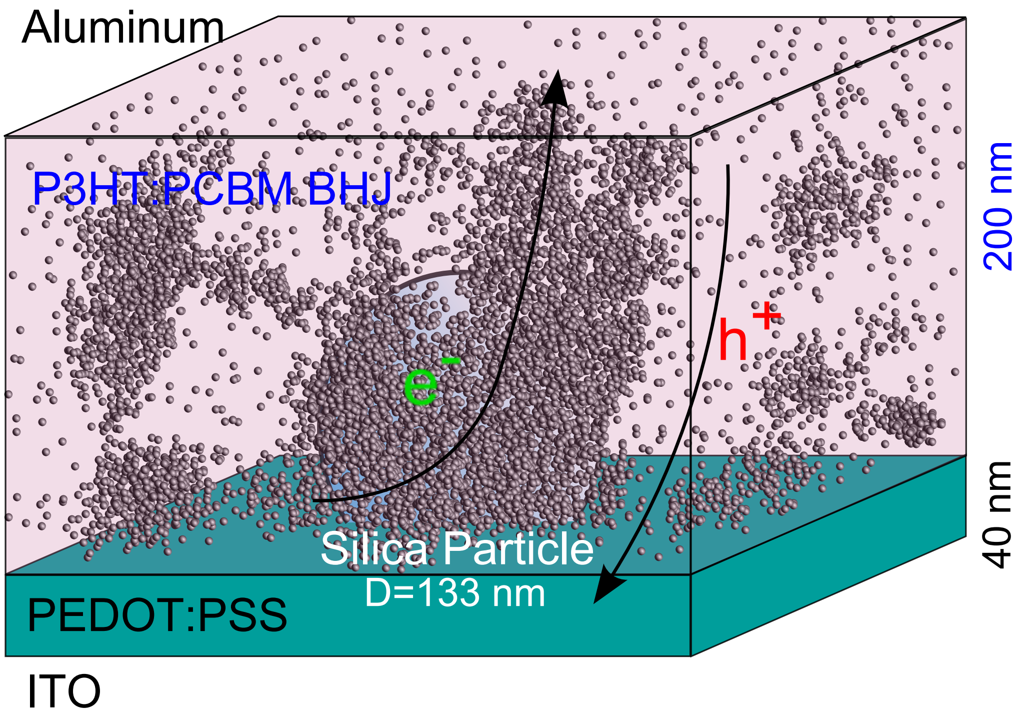

Fig. 11 Schematic illustration of the morphological impact of silica particles on the BHJ. The small dots represent the PCBM molecules with exaggerated size, but dimensions of the silica particle and the film thickness are scaled realistically. The red solid filling in the BHJ layer represents the matrix, which is the blend of crystalline and amorphous P3HT with dispersed PCBM. The crystalline P3HT cannot be distinguished by SANS, so it is also neglected in this cartoon for clarity. Some of the PCBM molecules are dispersed in the matrix shown as the individual dots, while some aggregates and forms the pure PCBM phase. The phase-separated PCBM is shown to concentrated around the silica particles by SANS, and is expected to aid electron transport across the active layer. Due to the local fluctuation in PCBM concentration, some other regions in the BHJ would be more depleted of PCBM, which may also provide a better environment for P3HT crystallization and make the hole transport more effective. These two effects reduce the series resistance and enhance the power conversion efficiency of the device.

ITO electrode, and increase the series resistance. However, the opposite observation in the series resistance strengthens our argument that those particles do not just occupy the working area of the electrode, but positively facilitate charge transport. From our observation with the SANS experiments, we strongly believe the PCBM is concentrated around the silica

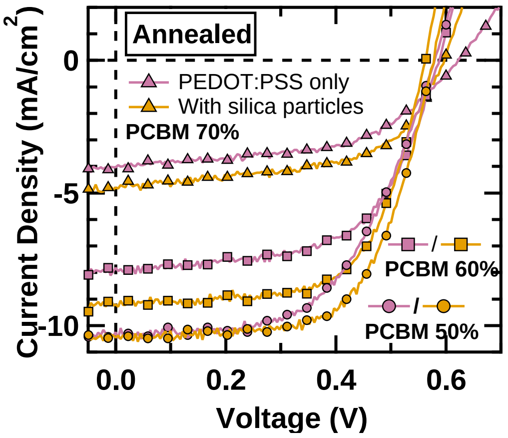

Fig. 10 IV curves of solar cells under AM 1.5 illumination.

particles to aid charge transport, which is illustrated in Fig. 11.

Our theory is that when PCBM is concentrated at the surface of the silica particles, it forms robust electron conductive pathways to reduce the internal resistance. Without the silica particles, the phase separation of PCBM may be initiated at the nucleation sites on the PEDOT:PSS substrate. It appears that PCBM is preferentially present at the bottom,[38–43] and can even grow into large crystals on the order of µm.[70,71] When the additional high-energy silica surface contacts the active layer, it can compete with the substrate for PCBM nucleation as part of the phase-transition. Because the thickness of PEDOT:PSS (40 nm) is less than the radius of a silica particle (67 nm) as shown in Fig. 11, more than half of the surface on the particle is extruded from the PEDOT:PSS. Therefore, 25 % of the device area covered by the particles is substituted with the extruded silica surface, which has at least twice the area of its underneath electrode. The introduced silica surface is certainly comparable to the amount of uncovered, planar PEDOT:PSS substrate, which accounts for 75 % of the device area. Therefore, a major portion of the PCBM is likely driven away from the horizontal substrate, and forced to form more useful vertical electron pathways around the silica particles.

Moreover, the local concentration of the PCBM around the silica particles implies other regions in the BHJ layer would become depleted of PCBM. Although PCBM does not intercalate into the P3HT crystal lattice and form a brand new bimolecular crystal,[72] much evidence has shown that concentrated PCBM hinders the crystallization of P3HT in the BHJ.[57,73,74] Therefore, the depletion of PCBM may be beneficial to the P3HT crystallization in those regions, which plays an important role in hole transport. In fact, we have attempted to quantify the P3HT crystallinity with a lab-size instrument using grazing incidence x-ray diffraction (GIXRD) (see Supporting Information). Unfortunately, because the silica strongly attenuates the x-ray signal, there is essentially no photon escaping from the dense forest of silica particles. Therefore, the reduction of the diffraction intensity of P3HT (100) peak is due to blocking of the photons near silica particles, and no useful information on the P3HT crystals can be obtained with this technique. Nevertheless, either the vertical organization of PCBM around the silica particles or the potentially better P3HT crystallinity in the PCBM-depleted regions are expected to be more effective when the BHJ has a higher PCBM concentration. Thus, the performance enhancement is pronounced when the PCBM content is equal to or greater than 50 Wt.%, the loading normally used for P3HT:PCBM,[75] as shown in Fig. 9 and Table 1.

Conclusion

The morphology of the P3HT:PCBM BHJ active layer is significantly influenced by the embedded 133 nm silica particles. We use a graphical method to study the SANS data of the active layer, and conclude that the reduction in the PCBM scattering intensity on the length scale of $\sim$30 nm is due to the depletion of phase-separated PCBM. Such depletion is a result of the formation of large PCBM structures at the high-energy surface of the silica particles. The PCBM-rich regions are postulated to provide better electron conducting pathways to reduce the series resistance of the devices. Specifically, for the devices with 50 to 70 Wt.% PCBM in the active layer, the series resistance is reduced by 30 to 50 %, and the PCE improved by 10 to 20 % compared to the respective control groups. This magnitude of improvement is comparable to that caused by surface plasmon resonance of the gold or silver NPs,[27,29,30,34] which does not exist with our silica particles. Therefore, the high-energy surface on the metal NPs may actually influence the device performance by as much as the plasmonic effect would do, and should not be ignored.

In addition, the improvement of the device performance by the silica particles is more pronounced when the concentration of PCBM is high, because the disorder with excessive PCBM may be effectively controlled. Such a strategy to manipulate the morphology deserves further investigation, as many of the high-performance polymers require high loading of fullerene derivatives.[32–34] One promising application of those large particles can be the improvement of the fullerene percolation between the electrodes, allowing a more efficient charge transport that is difficult to achieve in a thick BHJ active layer.[76] In conclusion, the use of high-energy particles provides an avenue for new designs of device architecture that may overcome the restriction of non-optimal morphology of the native BHJ, and helps to fully exercise the potential of the polymer.

Materials and Methods

Embedding of Silica Particles with the PEDOT:PSS Layer

Silica NPs with plain silicon oxide surfaces (Bangs Lab) were supplied in suspension. The particles were washed with deionized water (DIW) and ultrafiltrated via a cellulose filter with molecular weight cut-off at 10 000 g mol^{-1}. The washed product was stored for further use. The hydrodynamic diameter of the particles was 150 nm measured by dynamic light scattering, and the physical diameter was (124 ± 24) nm determined by SANS. Buffer layers of PEDOT:PSS (Clevios 4083, H. C. Starck) were used in all our devices. For the control group without the silica particles, PEDOT:PSS stock solution was diluted from 1.60 % to 1.38 % with DIW. The solution was spun-coated onto substrates at 3000 rpm and repeated three times to form 40 nm layers. For the experimental group with silica particles, 40 µL of the stock silica suspension (9.6 Wt.%) was mixed with 160 µL DIW and 800 µL stock PEDOT:PSS solution to yield 1 mL of mixture while maintaining the same dilution ratio as in the control group. The volume fraction of silica of this formulation is 0.139 % determined by SANS. The silica-PEDOT:PSS mixture was coated according to the same procedure described above. However, when the mixture was deposited onto an existing layer during the coating process, the PEDOT:PSS film is redissolved while the silica particles remain on the substrate. This provides an advantage to adjust the desirable particle density on the surface by changing the number of spin-coating operations.

Scanning Electron Microscopy

SEM studies were performed with a JSM-7400F microscope at the W. M. Keck Microscopy Facilities at the University of Delaware. The samples were sputtered with a layer of 5 nm gold-palladium alloy to improve the conductivity. To ensure uniform coverage of the silica particle across the surface and reproduciblility of the coating process, more than three independently prepared samples were measured. On each sample, at least twelve SEM images were taken on one sample at randomly chosen locations over a 6×6 mm^2 area. These images were analyzed using ImageJ software[77] to estimate the particle density per unit area, and the surface coverage was calculated using the projected area of each particle. We found the uncertainty of the particle density between the sampled regions is approximately 20 %, and select a representative image (Fig. 2 (a)) to analyze in great detail as described previously in the main text.

Device Fabrication and Characterization

ITO coated glass slides (8 to 12 Ω/□, Delta Technologies) were used as the substrates for the solar cells. They were cleaned by ultrasonication in acetone and isopropanol, followed by UV-ozone cleaning before being coated with silca-PEDOT:PSS layers as described above. The slides were dried at 130 °C in an oven and then transferred into a nitrogen-filled glove box, where the rest of the fabrication and characterization was performed. P3HT (P100 from Rieke Metals, 98 % regioregularity, molecular weight of 50 000 to 60 000 g mol^{-1}), PCBM (99 %, from Nano-C) and o-dichlorobenzene (99.8 % extra dry, Acros) were purchased and used without further purification. Stock solutions of P3HT and PCBM were prepared at the same concentration of 40 mg ml^{-1} in o-dichlorobenzene by heating the solution on a hot plate at 80 °C overnight. The stock solutions were cooled to room temperature and then mixed at designated weight ratios two hours prior to being deposited on the substrate. The solutions were spun-coated on the PEDOT:PSS coated substrates at 700 rpm, and then annealed on a 110 °C hot plate for 10 min. An electrode consisting of 1 nm lithium fluoride and 80 nm aluminum was subsequently deposited on top of the active layer by thermal evaporation at 1×10^{-6} torr. The working area of each solar cell is a 0.2 cm^2 rectangle, shaped by the acid-etched patterns on the ITO slides prior to the fabrication and the masking during electrode deposition. The testing of the device performance was conducted with a Keithley 2400 source meter under an AM 1.5G condition at 100 mW cm^{-2} illumination. The UV-Vis absorbance spectra were measured with a Shimadzu UV-3600 spectrometer in the transmission mode. All samples are coated on soda-lime glass substrates, whose absorption was subtracted as the background signal.

Small Angle Neutron Scattering

SANS was performed on the NG-3 and NG-7 beam lines at the National Institutes of Standards and Technology (NIST) Center for Neutron Research (NCNR) in Gaithersburg, MD, USA. The neutron wave length was 6 Å at detector distances of 1.3, 4 and 13 m, and 8 Å at 13 m with the focusing lens. Liquid samples were measured in quartz cells with a neutron path length of 1 mm at (20.0 ± 0.1) °C. The neutron scattering length density of silica was first determined with contrast matching experiments[78] as 3.65×10^{-6} Å^{-2}. For thin film samples of silica NPs coated with PEDOT:PSS and P3HT:PCBM layers, double-side polished silicon (100) wafers (Wafer World) were used as the substrates. Ten wafers carrying the thin films were stacked to increase the scattering intensity as described in detail elsewhere,[3,6], and on average 90 minutes of beam time was allocated on each sample. The absolute scattering intensity was obtained by comparison to the neutron flux of the main beam, and normalized according to the total thickness of the films or the quartz cell. For thin film samples, a stack of wafers coated with PEDOT:PSS were used as the empty cell and whose influence was subtracted from the data. The SANS data for annealed samples were taken on the same set of as-cast samples after annealing in the atmosphere at the beam line using the same protocol for the devices. This method minimized sample-to-sample variation in studying the effect of annealing, and reduced the sample preparation time and cost. All the model fitting procedures were performed with minimum least-square method using the package supplied by NCNR.[79]

Acknowledgement

This work was supported by NIST Award 70NANB10H256 through the Center for Neutron Science at the University of Delaware, and utilized facilities supported in part by the National Science Foundation under Agreement No. DMR-0944772. The authors acknowledge the support of the National Institute of Standards and Technology, U.S. Department of Commerce, in providing the neutron research facilities used in this work. The authors also thank Prof. David Martin for usage of the UV-Vis spectrometer.

Disclaimer

Certain commercial equipment, instruments, materials, suppliers, or software, are identified in this paper to foster understanding. Such identification does not imply recommendation or endorsement by the National Institute of Standards and Technology, nor does it imply that the materials or equipment identified are necessarily the best available for the purpose.

References

1 G. Li, R. Zhu and Y. Yang, *Nature Photonics*, 2012, **6**, 153–161.
2 B. C. Thompson and J. M. J. Fréchet, *Angewandte Chemie (International ed. in English)*, 2008, **47**, 58–77.
3 J. W. Kiel, A. P. R. Eberle and M. E. Mackay, *Physical Review Letters*, 2010, **105**, 168701.
4 K. Vakhshouri, D. R. Kozub, C. Wang, A. Salleo and E. D. Gomez, *Physical Review Letters*, 2012, **108**, 026601.
5 C. Guo, Y.-H. Lin, M. D. Witman, K. A. Smith, C. Wang, A. Hexemer, J. Strzalka, E. D. Gomez and R. Verduzco, *Nano letters*, 2013, **13**, 2957–63.
6 H. Shen, W. Zhang and M. E. Mackay, *Journal of Polymer Science Part B: Polymer Physics*, 2014, **52**, 387–396.
7 J.-T. Chen and C.-S. Hsu, *Polymer Chemistry*, 2011, **2**, 2707.
8 M. Helgesen, R. Sondergaard and F. C. Krebs, *Journal of Materials Chemistry*, 2010, **20**, 36–60.
9 J. J. F. Nijs, J. Szlufcik, J. Poortmans, S. Sivoththaman and R. P. Mertens, *IEEE Transactions on Electron Devices*, 1999, **46**, 1948–1969.
10 H. a. Atwater and A. Polman, *Nature Materials*, 2010, **9**, 205–13.
11 Q. Gan, F. J. Bartoli and Z. H. Kafafi, *Advanced Materials*, 2013, 2385–2396.
12 A. Polman, *Science*, 2008, **322**, 868–869.
13 V. E. Ferry, J. N. Munday and H. a. Atwater, *Advanced Materials*, 2010, **22**, 4794–808.
14 K. Kim and D. L. Carroll, *Applied Physics Letters*, 2005, **87**, 203113.
15 S.-S. Kim, S.-I. Na, J. Jo, D.-Y. Kim and Y.-C. Nah, *Applied Physics Letters*, 2008, **93**, 073307.
16 F.-C. Chen, J.-L. Wu, C.-L. Lee, Y. Hong, C.-H. Kuo and M. H. Huang, *Applied Physics Letters*, 2009, **95**, 013305.
17 J.-L. Wu, F.-C. Chen, Y.-S. Hsiao, F.-C. Chien, P. Chen, C.-H. Kuo, M. H. Huang and C.-S. Hsu, *ACS Nano*, 2011, **5**, 959–967.
18 D. D. S. Fung, L. Qiao, W. C. H. Choy, C. Wang, W. E. I. Sha, F. Xie and S. He, *Journal of Materials Chemistry*, 2011, **21**, 16349.
19 W.-J. Yoon, K.-Y. Jung, J. Liu, T. Duraisamy, R. Revur, F. L. Teixeira, S. Sengupta and P. R. Berger, *Solar Energy Materials and Solar Cells*, 2010, **94**, 128–132.
20 G. Spyropoulos, M. Stylianakis, E. Stratakis and E. Kymakis, *Photonics and Nanostructures - Fundamentals and Applications*, 2011, **9**, 184–189.
21 A. J. Morfa, K. L. Rowlen, T. H. Reilly, M. J. Romero and J. van de Lagemaat, *Applied Physics Letters*, 2008, **92**, 013504.
22 J. H. Lee, J. H. Park, J. S. Kim, D. Y. Lee and K. Cho, *Organic Electronics*, 2009, **10**, 416–420.
23 W. E. I. Sha, W. C. H. Choy, Y. G. Liu and W. Cho Chew, *Applied Physics Letters*, 2011, **99**, 113304.
24 J. Zhu, M. Xue, R. Hoekstra, F. Xiu, B. Zeng and K. L. Wang, *Nanoscale*, 2012, **4**, 1978–81.
25 K. Topp, H. Borchert, F. Johnen, a. V. Tunc, M. Knipper, E. von Hauff, J. Parisi and K. Al-Shamery, *The Journal of Physical Chemistry A*, 2010, **114**, 3981–9.
26 M. Xue, L. Li, B. J. Tremolet de Villers, H. Shen, J. Zhu, Z. Yu, A. Z. Stieg, Q. Pei, B. J. Schwartz and K. L. Wang, *Applied Physics Letters*, 2011, **98**, 253302.
27 G. D. Spyropoulos, M. M. Stylianakis, E. Stratakis and E. Kymakis, *Applied Physics Letters*, 2012, **100**, 213904.
28 B. Paci, G. D. Spyropoulos, A. Generosi, D. Bailo, V. R. Albertini, E. Stratakis and E. Kymakis, *Advanced Functional Materials*, 2011, **21**, 3573–3582.
29 B. Paci, A. Generosi, V. R. Albertini, G. D. Spyropoulos, E. Stratakis and E. Kymakis, *Nanoscale*, 2012, **4**, 7452–9.
30 C.-H. Kim, S.-H. Cha, S. C. Kim, M. Song, J. Lee, W. S. Shin, S.-J. Moon, J. H. Bahng, N. a. Kotov and S.-H. Jin, *ACS Nano*, 2011, **5**, 3319–25.
31 C. C. D. Wang, W. C. H. Choy, C. Duan, D. D. S. Fung, W. E. I. Sha, F.-X. Xie, F. Huang and Y. Cao, *Journal of Materials Chemistry*, 2012, **22**, 1206.
32 D. H. Wang, D. Y. Kim, K. W. Choi, J. H. Seo, S. H. Im, J. H. Park, O. O. Park and A. J. Heeger, *Angewandte Chemie (International ed. in English)*, 2011, **50**, 5519–23.
33 D. H. Wang, K. H. Park, J. H. Seo, J. Seifter, J. H. Jeon, J. K. Kim, J. H. Park, O. O. Park and A. J. Heeger, *Advanced Energy Materials*, 2011, **1**, 766–770.
34 H. Choi, J.-P. Lee, S.-J. Ko, J.-W. Jung, H. Park, S. Yoo, O. Park, J.-R. Jeong, S. Park and J. Y. Kim, *Nano Letters*, 2013, **13**, 2204–8.
35 J. Yang, J. You, C.-C. Chen, W.-C. Hsu, H.-r. Tan, X. W. Zhang, Z. Hong and Y. Yang, *ACS Nano*, 2011, **5**, 6210–7.
36 L. Lu, Z. Luo, T. Xu and L. Yu, *Nano Letters*, 2013, **13**, 59–64.
37 J. Szeremeta, M. Nyk, A. Chyla, W. Strek and M. Samoc, *Optical Materials*, 2011, **33**, 1372–1376.
38 M. Campoy-Quiles, T. Ferenczi, T. Agostinelli, P. G. Etchegoin, Y. Kim, T. D. Anthopoulos, P. N. Stavrinou, D. D. C. Bradley and J. Nelson, *Nature Materials*, 2008, **7**, 158–164.
39 D. S. Germack, C. K. Chan, B. H. Hamadani, L. J. Richter, D. a. Fischer, D. J. Gundlach and D. M. DeLongchamp, *Applied Physics Letters*, 2009, **94**, 233303.
40 D. S. Germack, C. K. Chan, R. J. Kline, D. a. Fischer, D. J. Gundlach, M. F. Toney, L. J. Richter and D. M. DeLongchamp, *Macromolecules*, 2010, **43**, 3828–3836.

41 D. S. Germack, A. Checco and B. M. Ocko, *ACS Nano*, 2013, **7**, 1990–9.

42 H. Wang, E. D. Gomez, J. Kim, Z. Guan, C. Jaye, D. A. Fischer, A. Kahn and Y.-l. Loo, *Chemistry of Materials*, 2011, **23**, 2020–2023.

43 A. Kumar, G. Li, Z. Hong and Y. Yang, *Nanotechnology*, 2009, **20**, 165202.

44 Z. Xu, L.-M. Chen, G. Yang, C.-H. Huang, J. Hou, Y. Wu, G. Li, C.-S. Hsu and Y. Yang, *Advanced Functional Materials*, 2009, **19**, 1227–1234.

45 A. F. Tillack, K. M. Noone, B. A. MacLeod, D. Nordlund, K. P. Nagle, J. A. Bradley, S. K. Hau, H.-L. Yip, A. K. Y. Jen, G. T. Seidler and D. S. Ginger, *ACS Applied Materials & Interfaces*, 2011, **3**, 726–732.

46 J. Alonzo, W. M. Kochemba, D. L. Pickel, M. Ramanathan, Z. Sun, D. Li, J. Chen, B. G. Sumpter, W. T. Heller and S. M. Kilbey, *Nanoscale*, 2013, **5**, 9357–64.

47 A. Orimo, K. Masuda, S. Honda, H. Benten, S. Ito, H. Ohkita and H. Tsuji, *Applied Physics Letters*, 2010, **96**, 043305.

48 D. Chen, A. Nakahara, D. Wei, D. Nordlund and T. P. Russell, *Nano Letters*, 2010, **11**, 561–567.

49 S. a. Mauger, L. Chang, S. Friedrich, C. W. Rochester, D. M. Huang, P. Wang and A. J. Moulé, *Advanced Functional Materials*, 2013, **23**, 1935–1946.

50 H.-C. Liao, C.-S. Tsao, T.-H. Lin, M.-H. Jao, C.-M. Chuang, S.-Y. Chang, Y.-C. Huang, Y.-T. Shao, C.-Y. Chen, C.-J. Su, U.-S. Jeng, Y.-F. Chen and W.-F. Su, *ACS Nano*, 2012, **6**, 1657–1666.

51 A. J. Parnell, A. D. F. Dunbar, A. J. Pearson, P. A. Staniec, A. J. C. Dennison, H. Hamamatsu, M. W. A. Skoda, D. G. Lidzey and R. A. L. Jones, *Advanced Materials*, 2010, **22**, 2444–2447.

52 J. W. Kiel, B. J. Kirby, C. F. Majkrzak, B. B. Maranville and M. E. Mackay, *Soft Matter*, 2010, **6**, 641–646.

53 T.-C. Tseng, E. S. McGarrity, J. W. Kiel, P. M. Duxbury, M. E. Mackay, A. L. Frischknecht, S. Asokan and M. S. Wong, *Soft Matter*, 2010, **6**, 1533–1538.

54 M. Kotlarchyk and S.-H. Chen, *The Journal of Chemical Physics*, 1983, **79**, 2461–2469.

55 N. E. Valadez-Pérez, R. Castañeda Priego and Y. Liu, *RSC Advances*, 2013, **3**, 25110.

56 M. C. Gurau, D. M. Delongchamp, B. M. Vogel, E. K. Lin, D. a. Fischer, S. Sambasivan and L. J. Richter, *Langmuir*, 2007, **23**, 834–42.

57 M.-Y. Chiu, U. S. Jeng, M.-S. Su and K.-H. Wei, *Macromolecules*, 2009, **43**, 428–432.

58 D. R. Kozub, K. Vakhshouri, L. M. Orme, C. Wang, A. Hexemer and E. D. Gomez, *Macromolecules*, 2011, **44**, 5722–5726.

59 M. Teubner and R. Strey, *The Journal of Chemical Physics*, 1987, **87**, 3195–3200.

60 C. G. Vonk, J. F. Billman and E. W. Kaler, *The Journal of Chemical Physics*, 1988, **88**, 3970–3975.

61 H.-C. Liao, C.-S. Tsao, T.-H. Lin, C.-M. Chuang, C.-Y. Chen, U. S. Jeng, C.-H. Su, Y.-F. Chen and W.-F. Su, *Journal of the American Chemical Society*, 2011, **133**, 13064–13073.

62 W. Yin and M. Dadmun, *ACS Nano*, 2011, **5**, 4756–4768.

63 K. Vakhshouri, S. V. Kesava, D. R. Kozub and E. D. Gomez, *Materials Letters*, 2013, **90**, 97–102.

64 M. E. Mackay, A. Tuteja, P. M. Duxbury, C. J. Hawker, B. Van Horn, Z. Guan, G. Chen and R. S. Krishnan, *Science*, 2006, **311**, 1740–3.

65 B. a. Collins, E. Gann, L. Guignard, X. He, C. R. McNeill and H. Ade, *The Journal of Physical Chemistry Letters*, 2010, **1**, 3160–3166.

66 B. A. Collins, J. R. Tumbleston and H. Ade, *The Journal of Physical Chemistry Letters*, 2011, **2**, 3135–3145.

67 N. D. Treat, M. a. Brady, G. Smith, M. F. Toney, E. J. Kramer, C. J. Hawker and M. L. Chabinyc, *Advanced Energy Materials*, 2011, **1**, 82–89.

68 H. Chen, R. Hegde, J. Browning and M. D. Dadmun, *Physical chemistry chemical physics : PCCP*, 2012, **14**, 5635–41.

69 G. W. Heffner and D. S. Pearson, *Macromolecules*, 1991, **24**, 6295–6299.

70 B. Watts, W. J. Belcher, L. Thomsen, H. Ade and P. C. Dastoor, *Macromolecules*, 2009, **42**, 8392–8397.

71 A. Swinnen, I. Haeldermans, P. Vanlaeke, J. D'Haen, J. Poortmans, M. D'Olieslaeger and J. V. Manca, *Eur. Phys. J. Appl. Phys.*, 2006, **36**, 251–256.

72 N. C. Miller, S. Sweetnam, E. T. Hoke, R. Gysel, C. E. Miller, J. a. Bartelt, X. Xie, M. F. Toney and M. D. McGehee, *Nano Letters*, 2012, **12**, 1566–70.

73 J. Zhao, A. Swinnen, G. Van Assche, J. Manca, D. Vanderzande and B. V. Mele, *The Journal of Physical Chemistry B*, 2009, **113**, 1587–1591.

74 S. Lilliu, T. Agostinelli, E. Pires, M. Hampton, J. Nelson and J. E. Macdonald, *Macromolecules*, 2011, **44**, 2725–2734.

75 M. T. Dang, L. Hirsch and G. Wantz, *Advanced Materials*, 2011, **23**, 3597–3602.

76 J. a. Bartelt, Z. M. Beiley, E. T. Hoke, W. R. Mateker, J. D. Douglas, B. a. Collins, J. R. Tumbleston, K. R. Graham, A. Amassian, H. Ade, J. M. J. Fréchet, M. F. Toney and M. D. McGehee, *Advanced Energy Materials*, 2013, **3**, 364–374.

77 C. a. Schneider, W. S. Rasband and K. W. Eliceiri, *Nature Methods*, 2012, **9**, 671–675.

78 A. P. R. Eberle, N. J. Wagner, B. Akgun and S. K. Satija, *Langmuir*, 2010, **26**, 3003–3007.

79 S. R. Kline, *Journal of Applied Crystallography*, 2006, **39**, 895–900.